Published in final edited form as:
Int J Funct Inform Personal Med. 2008 ; 1(2): 189–204. doi:10.1504/IJFIPM.2008.020187.

Impulse response and Modulation Transfer Function analysis for Shift-And-Add and Back Projection image reconstruction algorithms in Digital Breast Tomosynthesis (DBT)

Ying Chen,
Department of Electrical and Computer Engineering, Biomedical Engineering Graduate Program, Southern Illinois University, Carbondale IL 62901, USA, Duke Advanced Imaging Laboratories, Department of Biomedical Engineering, Duke University, Durham NC 27705, USA, E-mail: chen@engr.siu.edu

Joseph Y. Lo, and
Duke Advanced Imaging Laboratories, Department of Biomedical Engineering and Radiology, Medical Physics Graduate Program, Duke University, Durham NC 27705, USA, E-mail: joseph.lo@duke.edu

James T. Dobbins III
Duke Advanced Imaging Laboratories, Department of Biomedical Engineering and Radiology, Medical Physics Graduate Program, Duke University, Durham NC 27705, USA, E-mail: james.dobbins@duke.edu

Abstract

Breast cancer is second only to lung cancer as the leading cause of non-preventable cancer death in women. Digital Breast Tomosynthesis (DBT) is a promising technique to improve early breast cancer detection. In this paper, we present the impulse response and Modulation Transfer Function (MTF) analysis to quantitatively compare Shift-And-Add (SAA) and point-by-point Back Projection (BP) three-dimensional image reconstruction algorithms in DBT. A Filtered Back Projection (FBP) deblurring algorithm based on point-by-point BP was used to demonstrate deblurred tomosynthesis images.

Keywords

mammography; tomosynthesis; Shift-And-Add; SAA; Back Projection; BP; Filtered Back Projection; FBP; impulse response; Modulation Transfer Function; MTF

1 Introduction

This paper analyses and quantifies the impulse response and Modulation Transfer Function (MTF) of Shift-And-Add (SAA) and Back Projection (BP) image reconstruction algorithms in Digital Breast Tomosynthesis (DBT).

Breast cancer is second only to lung cancer as the leading cause of non-preventable cancer death in women. DBT has been considered as a promising technique to reconstruct three-

Correspondence to: Ying Chen.

Reference to this paper should be made as follows: Chen, Y., Lo, J.Y. and Dobbins III, J.T. (xxxx) 'Impulse response and Modulation Transfer Function analysis for Shift-And-Add and Back Projection image reconstruction algorithms in Digital Breast Tomosynthesis (DBT)', *Int. J. Functional Informatics and Personalised Medicine*, Vol. x, No. x, pp.xxx–xxx.

dimensional information of the breast to improve early breast cancer detection. Compared with standard mammography two-dimensional imaging techniques, DBT improves conspicuousness of structures by removing the visual clutter associated with overlying anatomy (Dobbins III and Godfrey, 2003; Chen et al., 2005; Niklason et al., 1997; Wu et al., 2003; Chen et al., 2007; Bissonnette et al., 2005; Zhang et al., 2006).

As early as 1932, Ziedses des Plantes (1932) led the pioneering effort in convention linear tomography. Grant (1972) developed conventional SAA tomosynthesis to reconstruct planes through the subject 40 years Until now, several DBT image reconstruction algorithms have been proved effectively by different research groups. In 1997, Niklason and colleagues reported image-stretching SAA technique for mammography to investigate a tomosynthesis method with the X-ray tube moved in an arc above the stationary breast and detector (Niklason et al., 1997). Suryanarayana et al. (2000 Suryanarayana et al. (2001) reported research on breast tomosynthesis with Webber's Tuned-Aperture Computed Tomography (TACT) algorithm in 2000. In 2003, Wu et al. (2003) applied the maximum likelihood iterative algorithm (MLEM) to reconstruct the distribution of X-ray attenuation in the breast. FBP algorithms have been used in breast tomosynthesis by a few groups (Chen et al., 2005, 2006a; Mertelemeier et al., 2006; Stevens et al., 2001; Lauritsch and Haerer, 1998; Matsuo et al., 1993). Matrix Inversion Tomosynthesis (MITS) was originally invented by Dobbins at Duke University (Dobbins III, 1990). It has been investigated in tomography of the lung (Godfrey et al., 2006) and arthritis assessment (Duryea et al., 2003). In 2004, we reported MITS application in breast tomosynthesis (Chen et al., 2004). During 2005–2007, we have reported research results on MITS, FBP and Gaussian Frequency Blending (GFB) algorithms for breast tomosynthesis image reconstruction (Chen et al., 2005, 2006a, 2007c).

Among available algorithms, the traditional SAA is a method to calculate the shift amount along the X-ray tube's motion direction to line-up in-plane structures and suppress out-of-plane artefacts (Dobbins III and Godfrey, 2003; Chen et al., 2005). It also works as the foundation of a few other algorithms, including Niklason and colleagues' image stretching SAA (Niklason et al., 1997), TACT (Suryanarayanan et al., 2000, 2001), MITS (Chen et al., 2004, 2005), etc. Currently, most commercial breast tomosynthesis prototype devices apply the isocentric tube motion geometry where the X-ray tube moves along an arc above the detector (Wu et al., 2003; Bissonnette et al., 2005; Zhang et al., 2006). With isocentric motion of DBT, the shift amount actually occurs in both the X-ray tube's motion direction and the direction perpendicular to tube motion direction. Under this situation, approaches based on traditional SAA method are not enough for an accurate image reconstruction of the breast. As a result, morphology of structures such as micro-calcifications appears slightly blurred (Chen et al., 2007a).

In this paper, datasets of tomosynthesis projection images were simulated. The imaging geometry of a Siemens selenium-based direct conversion Mammomat Novation prototype system (Bissonnette et al., 2005) were used to simulate tomosynthesis projection images. Impulse response and MTF on three-dimensional reconstructed images were analysed to compare traditional SAA and BP algorithms. A Filtered Back Projection (FBP) deblurring algorithm (Chen et al., 2005, 2006a) was further applied to the BP algorithm to demonstrate the deblurred tomosynthesis images, as they would normally be portrayed to observers.

2 Methods

2.1 Tomosynthesis image reconstruction algorithms

Traditional SAA calculates the shift amount along the X-ray tube's motion direction one-dimensionally (Dobbins III and Godfrey, 2003; Chen et al., 2005). When the X-ray tube moves, structures at different locations will be projected onto the detector at different

positions according to relative heights of the objects. In order to reconstruct slice images of the breast at a specific height above the detector, each projection image was shifted by an amount appropriate for the plane of reconstruction.

Figure 1 shows the geometry of a Siemens tomosynthesis imaging acquisition system that we used (Bissonnette et al., 2005). Point O represents the rotation centre that is 60 mm above the detector. SID represents the X-ray source to image distance. A compression paddle was used to keep the object still. Plane j represents the reconstruction plane located at a height of Z above the detector. T_0 represents X-ray tube's middle (0°) location. When the X-ray tube moves to T_i location, the central point on plane j will be projected onto the detector with a position of S_i.

With traditional SAA algorithm, the entire projection image for T_i tube location will be shifted with an amount of S_i that can be computed as

$$S_i(Z)=\frac{Z\cdot \mathrm{ArmLength}\cdot \sin\theta}{(\mathrm{SID}-\mathrm{ArmLength}-Z)+\mathrm{ArmLength}\cdot\cos\theta} \quad (1)$$

where 'Arm Length' means the length of rotation arm, which is equal to the distance from the rotation centre O to the tube location T_0 or T_i.

The shifted projection images were added together to line up structures in in-focus plane and blur out structures in other planes (Dobbins III and Godfrey, 2003; Chen et al., 2005). The reconstructed slice image at plane j can be calculated as:

$$T(x,y,Z)=\frac{1}{N}\sum_{i=1}^{N} I_i(x,y)\otimes\delta[y-S_i(Z)] \quad (2)$$

where y direction represents the tube's motion direction. $I_i(x, y)$ represents the projection image when the X-ray tube moves to T_i location. N is the total number of projection images of the tomosynthesis sequence.

Point-by-point BP calculates the exact two-dimensional projected location for each pixel on reconstructed planes at a certain height above the detector (Chen et al., 2007a; Wu et al., 2004). As shown in Figure 2, the X-ray tube is located above the chest wall. Point A represents a single structure on a reconstruction plane. When the X-ray tube moves along y direction to locations of T_1, T_2, … T_n above the detector, point A will be projected onto the detector with locations of S_1, S_2, … through S_n correspondingly. The projection path of S_1, S_2, … S_n actually follows a two-dimensional arc rather than a one-dimensional line along y direction. With point-by-point BP, the shift amount along both x and y axes were calculated. All involved image values on contributing projection images were then added together and back projected to generate reconstruction images (Chen et al., 2007a, 2007b).

2.2 Impulse response and Modulation Transfer Function analysis

In order to compare traditional SAA and point-by-point BP, a ray-tracing method (Chen et al., 2007a) was used to simulate tomosynthesis projection images of a single delta function. Impulse response and MTF at different three-dimensional locations were analysed to evaluate the sharpness of reconstructed in-plane structures and the out-of-plane performance.

Geometries of Siemens tomosynthesis imaging acquisition system modified from a selenium-based Siemens Mammomat Novation prototype system (Bissonnette et al., 2005)

were used to simulate tomosynthesis projection images. Tomosynthesis datasets with 49, 25 and 13 projection images of a delta function (impulse) were simulated with a total angular range of ±25° and ±12.5° (with respect to the rotation centre that is 60 mm above the detector) of the simulated X-ray point source. Four different impulse locations were considered:

- an impulse that is exactly underneath the X-ray source (near the chest wall) and in a defined plane (40 mm above the detector surface cover)
- an impulse that is exactly underneath the X-ray source (near chest wall) and halfway between reconstructed planes (37.5 mm above the detector surface)
- an impulse that is approximately 4 cm away from the chest wall and in a defined reconstructed plane (40 mm above the detector surface)
- an impulse that is approximately 4 cm away from the chest wall and halfway between reconstructed planes (37.5 mm above the detector surface).

Background $1/r^2$ exposure variations were taken into account where r is the distance from the projection point to the X-ray point source (Chen et al., 2007a).

The simulated tomosynthesis datasets of projection images were then reconstructed by traditional SAA and point-by-point BP algorithms. The image size was 2048 × 2048 with a pixel size of 85 μm. In-plane impulse responses on the reconstruction plane (40 mm above the detector surface cover) and out-of-plane responses (35 mm above the detector surface cover) were analysed and compared. The impulse responses were normalised based on the ideal condition when the impulse is exactly located underneath the X-ray source (Chen et al., 2007a). MTF was computed as a normalised two-dimensional Fourier Transform of the impulse responses at reconstruction planes (Chen et al., 2007c; Chen, 2007).

2.3 Filtered Back Projection based on point-by-point BP

Because deblurring is important in producing high quality tomosynthesis images (Dobbins III and Godfrey, 2003), we applied a deblurring FBP algorithm to the point-by-point BP images (Chen et al., 2005; 2006a). The deblurring filters were based on the central slice theorem and Fourier frequency sampling density. The sampling density was calculated as the inverse of the shortest distance from a sampled point in Fourier space to sampled points from another view. Hamming and Gaussian filters were designed and used in conjunction with filters to control high frequency noise. The deblurring technique was performed on each projection image, after which the point-by-point BP algorithm was used to line up in-focus structures, taking into account the magnification and correction factors of the X-ray tube's isocentric motion.

3 Results

3.1 Impulse response and Modulation Transfer Function analysis

Figures 3–8 show the impulse response and MTF results with a simulated impulse located in a defined reconstruction plane at 40 mm above the detector, and approximately 4 cm away from the chest wall. Figures 3 and 4 show results from simulated acquisition parameters of 49 projections and ±25° total tube angular movement (with respect to the rotation *centre*). Figures 5 and 6 show results from 25 projections and ±12.5° angular movement (with respect to the rotation *centre*). Figures 7 and 8 show results from 13 projections and ±25° angular range.

Figures 9 and 10 show results with a simulated impulse located in a defined reconstruction plane at 40 mm above the detector, and underneath the X-ray source (near the chest wall).

Figure 11 show results with a simulated impulse that is approximately 4 cm away from the chest wall and halfway between reconstructed planes (37.5 mm above the detector surface). The simulated acquisition parameters of 49 projections and ±25° angular range were used in Figures 9–11.

On Figures 3–10, (a) and (b) give the impulse response and MTF, respectively, of reconstruction planes 5 mm lower than the impulse's location; (c) and (d) give corresponding values in a plane at the exact height of the impulse's location. Figures 3, 5, 7, and 9 are results from traditional SAA, and Figures 4, 6, 8 and 10 are results from point-by-point BP. Figure 11(a) and (b) give results with traditional SAA at a reconstruction plane 2.5 mm below the impulse location; 11(c) and (d) give corresponding values with point-by-point BP.

In all graphs of impulse responses, the x and y axes give the pixel location on the reconstruction plane, and the plot displays the normalised amplitude of the response. The u and v axes are the spatial frequencies conjugate to x and y. For all graphs of impulse response, only a 40 × 40 pixel region close to the impulse was shown for clarity. For MTF, the whole spatial frequency range is shown.

One can see that with traditional SAA, when the impulse is away from the chest wall and the X-ray source moves along an angular range of ±25°, the in-plane response is noticeably blurred in a direction that is perpendicular to the direction of tube motion (Figures 3(c) and 7(c)). With traditional SAA, the out-of-plane responses are curved (Figures 3(a) and 7(a)), reflecting the uncorrected partial isocentric tube motion. With point-by-point BP, the in-plane response is much sharper (Figures 4(c) and 8(c)), and the out-of-plane blur responses change from curved to straight (Figures 4(a) and 8(a)). Compared with traditional SAA, the MTF performance of point-by-point BP is much smoother (Figure 4 vs. Figure 3, Figure 8 vs. Figure 7).

For traditional SAA, the in-plane orthogonal blur is less obvious for the narrower angular range of ±12.5° (Figure 5(c)) than for ±25° (Figures 3(c), 7(c)), but the curved out-of-plane response exists even at ±12.5° (Figure 5(a)). When the number of projection images decreases to be 13, the out-of-plane blur becomes discrete (Figures 7(a), 8(a)) due to limited projection numbers.

When the impulse is located near the chest wall, there is only a small difference between traditional SAA and point-by-point BP (Figures 9 and 10). However, one can still find that the in-plane response of point-by-point BP is a little higher than that of traditional SAA (Figures 9(c) and 10(c)).

When the impulse is located halfway between reconstructed planes (Figure 11), results similar to those described above for out-of-plane blur can be observed. The out-of-plane response of traditional SAA is curved while that of point-by-point BP is straight (Figure 11(a) and (c)). The MTF plot of point-by-point BP is much smoother than that of SAA (Figure 11(b) and (d)).

3.2 Human subject images

Figure 12 shows comparisons of a reconstructed region of interest (ROI) of a human breast by traditional SAA and point-by-point BP methods. A 7.99 × 7.99 mm reconstruction region containing a round-shaped calcification is demonstrated. The human subject image was acquired with our prototype breast tomosynthesis system under an IRB-approved protocol. A tomosynthesis sequence was acquired with 25 projection images and a total angular range of ±25° at the rotation *centre*. A technique of W/Rh spectrum/filtration with 28 kVp was

used, and the total dose of the tomosynthesis was same as the conventional mammogram (Chen et al., 2007a; Samei et al., 2005).

In Figure 12, compared with traditional SAA (Figure 12(e)), the round-shaped calcification was sharper and clearer in the point-by-point BP in-plane reconstruction (Figure 12(b)). The curved out-of-plane blur is clearly visible with traditional SAA in this case too (Figure 12(d), (f)).

Figure 13 is a low dose middle projection image of the same human breast when the X-ray tube was positioned at the 0° position. Figure 14 is the reconstructed slice image at a height of 7.5 mm above the detector surface cover, with our filtered FBP deblurring algorithm based on point-by-point BP. The deblurred point-by-point BP image (Figure 14) demonstrates better rendition of breast anatomy out to the skin line (Figure 13).

4 Discussion

With isocentric motion of X-ray tube in breast tomosynthesis, the X-ray tube's movement does not fall into a plane that is parallel to the detector plane. The track of projected locations of objects occurs in an arc along both the X-ray tube's motion direction and a direction perpendicular to tube's motion direction. With traditional SAA, the shift amount for each projection image is calculated only along the tube's motion direction. The in-plane structures are blurred. Moreover, the magnification of objects on the reconstruction plane varies from pixel-to-pixel. The isocentric motion of X-ray tube in DBT also introduces variable magnification.

Illustrations with impulse responses, MTF, and reconstructed human subject images showed that this is an inherent problem of traditional SAA with breast tomosynthesis. When the impulse was close to the chest wall and with narrower tube angular movement range of ±12.5°, traditional SAA could tolerate by showing less obvious blurry artefacts. However, when the object was 4 cm away from the chest wall and with wider angular range of ±25°, problems existed. Therefore, with traditional SAA, objects such as micro-calcifications appear slightly blurred in the direction perpendicular to the direction of tube motion, and their morphology changes (Chen et al., 2006b, 2007a).

The morphology changes coming from the isocentric X-ray tube's movement are corrected with a point-by-point BP algorithm. The in-plane structures are sharper. Point-by-point BP also addresses the issue of variable magnification by calculating shift amount for each pixel according to the exact location of the pixel in the reconstruction slices.

A FBP deblurring the reconstruction image based on point-by-point BP was illustrated to evaluate whether deblurring filters gave reasonable results with point-by-point BP (even though not perfectly spatially invariant). Although not completely spatially invariant, this approach subjectively did a good job of effective deblurring with point-by-point BP and was fast compared with iterative methods (Wu et al., 2003; Zhang et al., 2006). Results with human subjects demonstrated subjectively that FBP deblurring with point-by-point BP provides good rendition of detailed structures, reduced out-of-plane blur, and suppressed high frequency noise. Other deblurring algorithms, such as MITS (Chen et al., 2004, 2005), may also prove effective, though not perfectly, in this spatially non-invariant environment, and will be investigated in the future.

4 Conclusion

This paper analysed the impulse response and MTF of traditional SAA and point-by-point BP. It demonstrated the importance of using a point-by-point BP correction of isocentric

motion artefacts in tomosynthesis imaging of the breast, where the morphology of micro-calcifications bears a significant meaning in clinical decision making. Compared with traditional SAA, point-by-point BP improves the sharpness and rendition of morphology of structures such as micro-calcifications. Point-by-point BP provides better-focused in-plane response and less curvature artefacts. Issues of variable magnifications associated with isocentric motion of DBT are also addressed by point-by-point BP. Our example of FBP reconstructions based on point-by-point BP shows better rendition of breast anatomy and good rendition of detailed structures and suppressed out-of-plane artefacts. The point-by-point BP rather than traditional SAA should be considered as the foundation for further deblurring algorithms.

Acknowledgments

We thank Jay A. Baker, M.D., at Duke University Medical Center for clinical insight and helpful discussions. This work was supported by a grant from US Army Breast Cancer Research Program (USAMRMC W81XWH-06-1-0462), a research grant from Siemens Medical Solutions, and NIH/NCI R01 112437.

Biographies

Ying Chen holds a PhD Degree and is an Assistant Professor in the Department of Electrical and Computer Engineering at Southern Illinois University, Carbondale, IL. She received her PhD in Biomedical Engineering from Duke University in 2007. Her research interests are in the areas of digital tomosynthesis, image reconstruction algorithms and imaging parameters optimisation.

Joseph Y. Lo holds a PhD Degree and is an Assistant Professor of Biomedical Engineering, Radiology, and Medical Physics at Duke University and Duke University Medical Center. He received his PhD in Biomedical Engineering from Duke University in 1993. His research interests are in the areas of breast tomosynthesis and computer aided diagnosis.

James T. Dobbins III, holds a PhD Degree and is an Associate Professor of Biomedical Engineering, Radiology, and Medical Physics, and the Director of the Medical Physics Graduate Program at Duke University and Duke University Medical Center. He received his PhD in Physics from the University of Wisconsin-Madison in 1985. His recent academic interests include digital tomosynthesis and dual-energy digital radiography technique to improve diagnostic accuracy in digital chest radiography and digital mammography.

References

Bissonnette BM, Hansroul M, Masson E, Savard S, Cadieux S, Warmoes P, Gravel D, Agopyan J, Polischuk BT, Haerer WH, Mertelmeier T, Lo JY, Chen Y, Dobbins JT III, Jesneck JL, Singh S. Digital breast tomosynthesis using an amorphous selenium flat panel detector. Proc SPIE. 2005; 5745:529–540.

Chen, Y. PhD dissertation. Duke University; 2007. Digital Breast Tomosynthesis (DBT) – A Novel Imaging Technology to Improve Early Breast Cancer Detection: Implementation, Comparison and Optimization.

Chen, Y.; Lo, JY.; Dobbins, JT, III. Matrix Inversion Tomosynthesis (MITS) of the Breast: Preliminary Results in RSNA 90th Scientific Assembly; Chicago, IL. 2004.

Chen Y, Lo JY, Dobbins JT III. Impulse response analysis for several digital tomosynthesis mammography reconstruction algorithms. Proc SPIE. 2005; 5745:541–549.

Chen Y, Lo JY, Dobbins JT III. Two-dimensional shift-and-add algorithm for digital breast tomosynthesis reconstruction. Med Phys. 2006b; 33(6):2001.

Chen Y, Lo JY, Dobbins JT III. Importance of point-by-point back projection correction for isocentric motion in digital breast tomosynthesis: Relevance to morphology of structures such as microcalcifications. Med Phys. 2007a; 34(10):3885–3892. [PubMed: 17985634]

Chen Y, Lo JY, Dobbins JT III. A comparison between traditional shift-and add (SAA) and point-by-point Back Projection (BP) – relevance to morphology of microcalcifications for isocentric motion in Digit Breast Tomosynthesis (DBT). Proceedings of the 7th IEEE International Conference on Bioinformatics and Bioengineering. 2007b; I:563–568.

Chen Y, Lo JY, Baker JA, Dobbins JT III. Gaussian frequency blending algorithm with Matrix Inversion Tomosynthesis (MITS) and Filtered Back Projection (FBP) for better digital breast tomosynthesis reconstruction. Proc SPIE. 2006a; 6142:122–130.

Chen Y, Lo JY, Ranger NT, Samei E, Dobbins JT III. Methodology of NEQ(f) analysis for optimization and comparison of digital breast tomosynthesis acquisition techniques and reconstruction algorithms. Proc SPIE. 2007c; 6510:65101–I.

Dobbins, JT, III. Matrix Inversion Tomosynthesis Improvements in Longitudinal X-ray Slice Imaging. Duke University; USA: 1990. US Patent #4,903,204

Dobbins JT III, Godfrey DJ. Digital X-ray tomosynthesis: current state of the art and clinical potential. Phys Med Biol. 2003; 48:65–106.

Duryea J, Dobbins JT III, Lynch JA. Digital tomosynthesis of hand joints for arthritis assessment. Med Phys. 2003; 30(3):325–333. [PubMed: 12674232]

Godfrey DJ, McAdams HP, Dobbins JT III. Optimization of the matrix inversion tomosynthesis (MITS) impulse response and modulation transfer function characteristics for chest imaging. Med Phys. 2006; 33(3):655–667. [PubMed: 16878569]

Grant DG. Tomosynthesis: a three-dimensional radiographic imaging technique. IEEE Transactions on Biomedical Engineering. 1972; BME-19:20–28. [PubMed: 5008409]

Lauritsch G, Haerer W. A theoretical framework for filtered back-projection in tomosynthesis. Proc SPIE. 1998; 3338:1127–1137.

Matsuo H, Iwata A, Horiba I, Suzumura N. Three-dimensional image reconstruction by digital tomosynthesis using inverse filtering. IEEE Trans Med Imaging. 1993; 12:307–313. [PubMed: 18218419]

Mertelemeier T, Orman J, Haerer W, Dudam MK. Optimizing filtered backprojection reconstruction for a breast tomosynthesis prototype device. Proc SPIE. 2006; 6142:131–142.

Niklason LT, Christina BT, Niklason LE, Kopans DB, Castleberry DE, Opsahl-Ong BH, Landberg CE, Dejule MC, Fitzgerald PF, Fobare DF, Giambattista BW, Kwasnick RE, Liu J, Lubowski SJ, Possin GE, Richotte JF, Wei C, Wirth RF. Digital tomosynthesis in breast imaging. Radiology. 1997; 205:399–406. [PubMed: 9356620]

Samei, E.; Dobbins, JT., III; Lo, JY.; Tornai, MP. A Framework for Optimizing the Radiographic Technique in Digital X-ray Imaging in Radiation Protection Dosimetry. Oxford University Press; Oxford: 2005.

Stevens GM, Fahrig R, Pelc NJ. Filtered backprojection for modifying the impulse response of circular tomosynthesis. Med Phys. 2001; 28:372–380. [PubMed: 11318319]

Suryanarayanan S, Karellas A, Vedantham S, Baker SP, Glick SJ, D'Orsi CJ, Baker SP, Webber RL. Evaluation of linear and nonlinear tomosynthetic reconstruction methods in digital mammography. Acad Radiol. 2001; 8:219–224. [PubMed: 11249085]

Suryanarayanan S, Karellas A, Vedantham S, Glick SJ, D'Orsi CJ, Baker SP, Webber RL. Comparison of tomosynthesis methods used with digital mammography. Acad Radiol. 2000; 7:1085–1097. [PubMed: 11131053]

Wu T, Kopans DB, Eberhard JW, Opsahl-Ong B, Niklason L, Williams MB. Tomographic mammography using a limited number of low-dose cone-beam projection images. Med Phys. 2003; 30:365–380. [PubMed: 12674237]

Wu T, Moore RH, Rafferty EA, Kopans DB. A comparison of reconstruction algorithms for breast tomosynthesis. Med Phys. 2004; 9:2636–2647. [PubMed: 15487747]

Zhang Y, Chan H, Sahiner B, Wei J, Goodsitt MM, Hadjiiski LM, Ge J, Zhou C. A comparative study of limited-angle cone-beam reconstruction methods for breast tomosynthesis. Med Phys. 2006; 33(10):3781–3795. [PubMed: 17089843]

Ziedses des Plantes BG. Eine neue methode zur differenzierung in der roentgenographie (planigraphie). Acta Radiologica. 1932; 13:182–192.

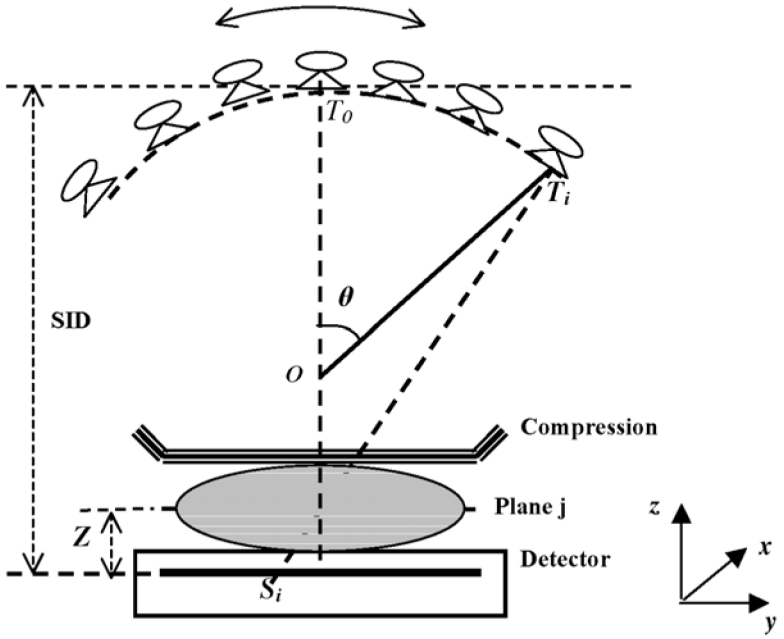

Figure 1.
Breast tomosynthesis system. The X-ray tube moves along an arc above the detector. *O* is the rotation centre

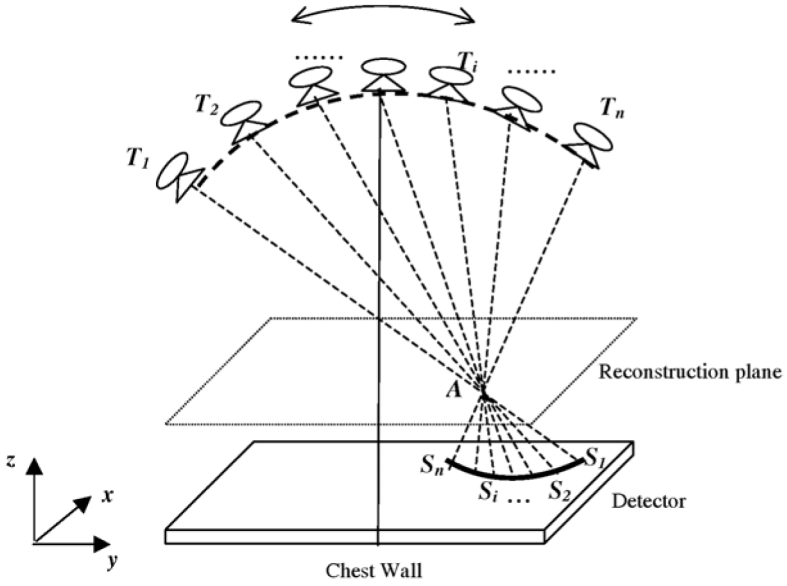

Figure 2.

Point-by-point Back Projection (BP) image reconstruction. The X-ray tube is located above the chest wall. When the X-ray tube moves to T_1, T_2,… T_n, point A on the reconstruction plane will be projected at S_1, S_2, … S_n on the detector correspondingly

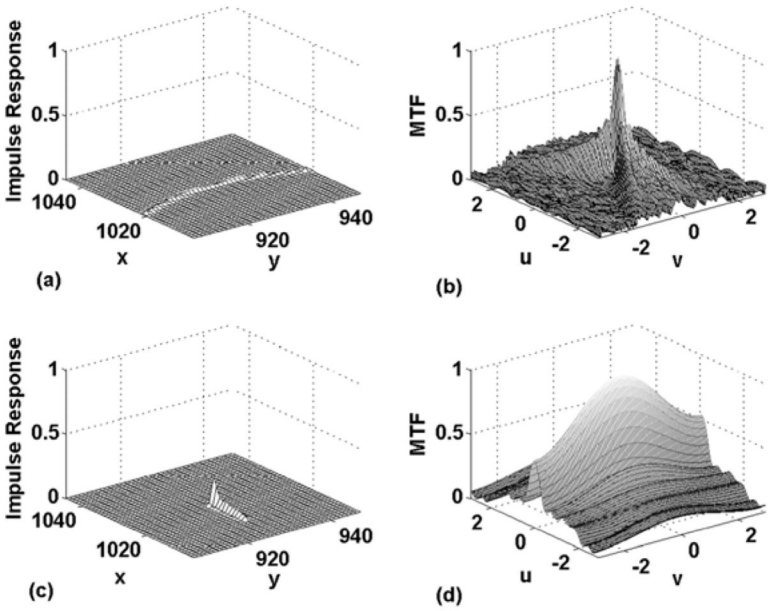

Figure 3.

Traditional SAA impulse response and MTF: 49 projection images and ±25° angular range, with the impulse located 40° mm above the detector and about 4 cm away from the chest wall. (a) and (b) give the impulse response and MTF, respectively, at a reconstruction plane 5 mm below the impulse location; (c) and (d) give corresponding values in a plane at the exact height of the impulse's location

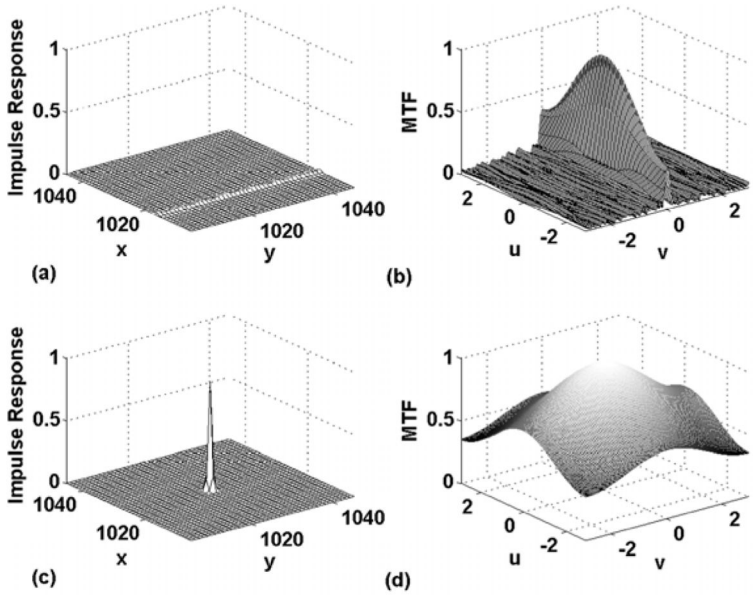

Figure 4.

Point-by-point BP impulse response and MTF: 49 projection images and ±25° angular range, with the impulse located 40 mm above the detector and about 4 cm away from the chest wall. (a) and (b) give the impulse response and MTF, respectively, at a reconstruction plane 5 mm below the impulse location; (c) and (d) give corresponding values in a plane at the exact height of the impulse's location

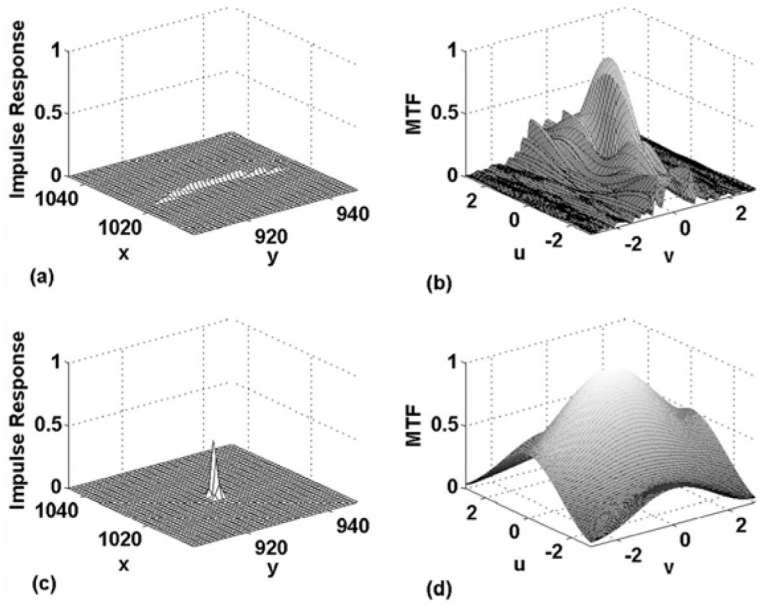

Figure 5.

Traditional SAA impulse response and MTF: 25 projection images and ±12.5° angular range, with the impulse located 40 mm above the detector and about 4 cm away from the chest wall. (a) and (b) give the impulse response and MTF, respectively, at a reconstruction plane 5 mm below the impulse location; (c) and (d) give corresponding values in a plane at the exact height of the impulse's location

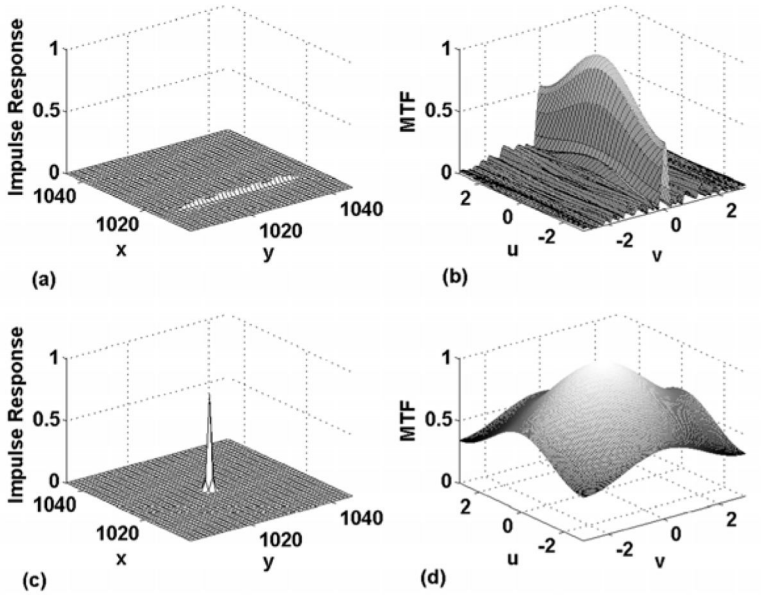

Figure 6.

Point-by-point BP impulse response and MTF: 25 projection images and ±12.5° angular range, with the impulse located 40 mm above the detector and about 4 cm away from the chest wall. (a) and (b) give the impulse response and MTF, respectively, at a reconstruction plane 5 mm below the impulse location; (c) and (d) give corresponding values in a plane at the exact height of the impulse's location

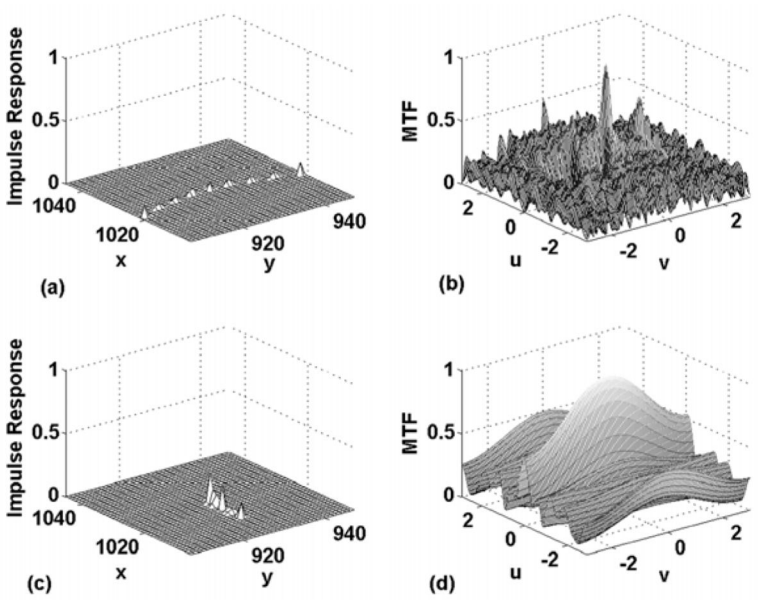

Figure 7.

Traditional SAA impulse response and MTF: 13 projection images and ±25° angular range, with the impulse located 40 mm above the detector and about 4 cm away from the chest wall. (a) and (b) give the impulse response and MTF, respectively, at a reconstruction plane 5 mm below the impulse location; (c) and (d) give corresponding values in a plane at the exact height of the impulse's location

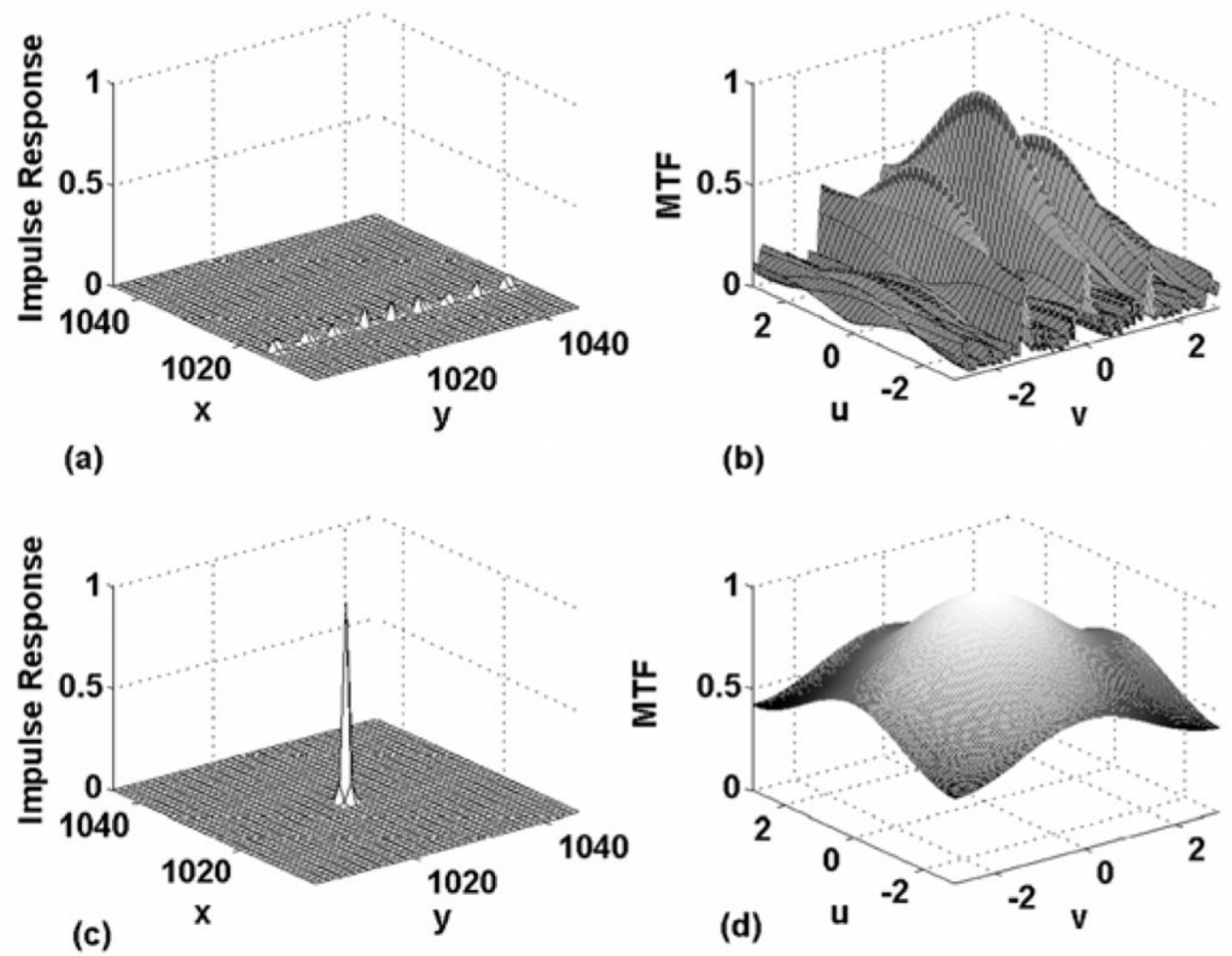

Figure 8.

Point-by-point BP impulse response and MTF: 13 projection images and ±25° angular range, with the impulse located 40 mm above the detector and about 4 cm away from the chest wall. (a) and (b) give the impulse response and MTF, respectively, at a reconstruction plane 5 mm below the impulse location; (c) and (d) give corresponding values in a plane at the exact height of the impulse's location

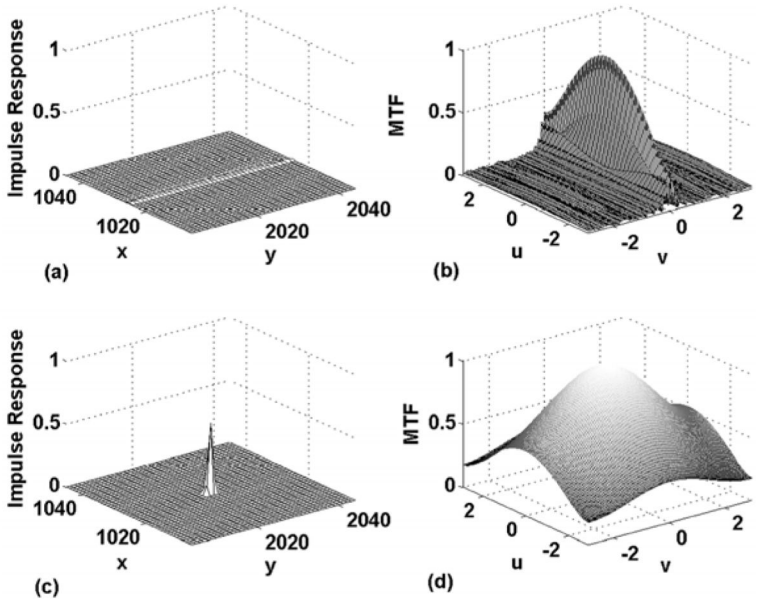

Figure 9.

Traditional SAA impulse response and MTF: 49 projection images and ±25° angular range, with the impulse located 40 mm above the detector and near the chest wall. (a) and (b) give the impulse response and MTF, respectively, at a reconstruction plane 5 mm below the impulse location; (c) and (d) give corresponding values in a plane at the exact height of the impulse's location

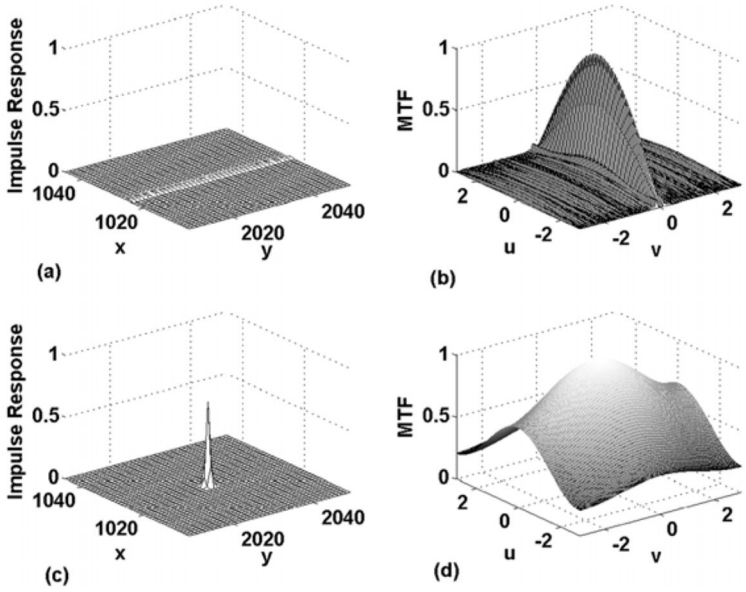

Figure 10.

Point-by-point BP impulse response and MTF: 49 projection images and ±25° angular range, with the impulse located 40 mm above the detector and near the chest wall. (a) and (b) give the impulse response and MTF, respectively, at a reconstruction plane 5 mm below the impulse location; (c) and (d) give corresponding values in a plane at the exact height of the impulse's location

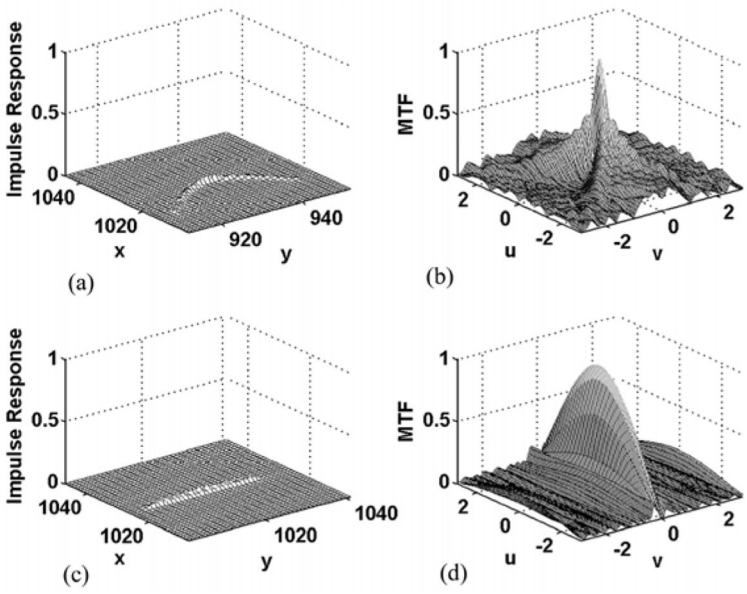

Figure 11.

Traditional SAA and point-by-point BP impulse responses and MTFs: 49 projection images and ±25° angular range, with the impulse located 37.5 mm above the detector and about 4 cm away from the chest wall. (a) and (b) give the traditional SAA impulse response and MTF, respectively, at a reconstruction plane 2.5 mm below the impulse location; (c) and (d) give corresponding values with point-by-point BP

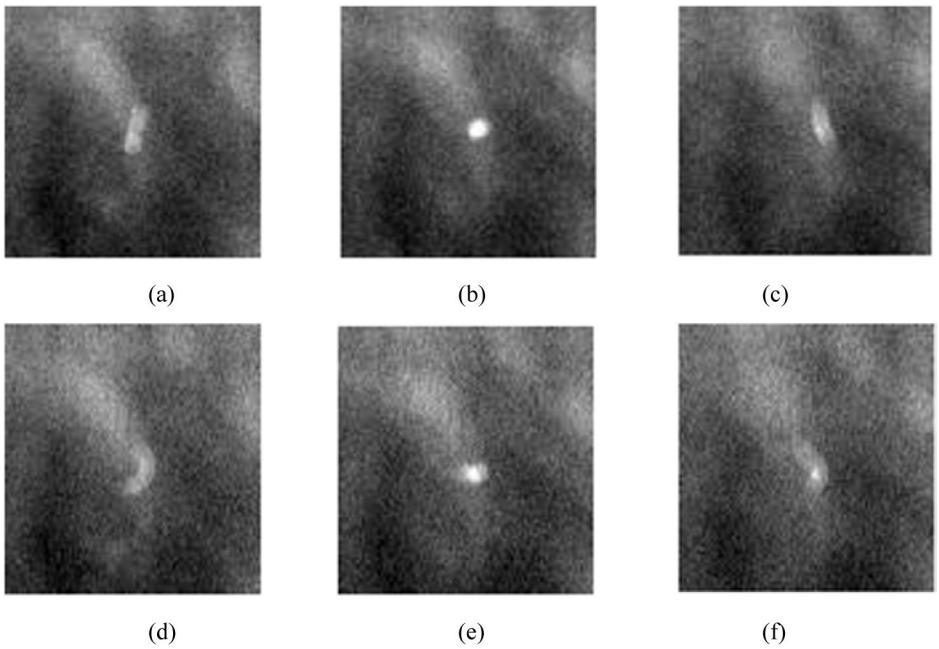

Figure 12.
Reconstructed 7.99 × 7.99 mm ROI of a human breast containing a calcification: (a) point-by-point BP, $Z = 25.5$ mm; (b) point-by-point BP, $Z = 27$ mm; (c) point-by-point BP, $Z = 28.5$ mm; (d) traditional SAA, $Z = 25.5$ mm; (e) traditional SAA, $Z = 27$ mm and (f) traditional SAA, $Z = 28.5$ mm

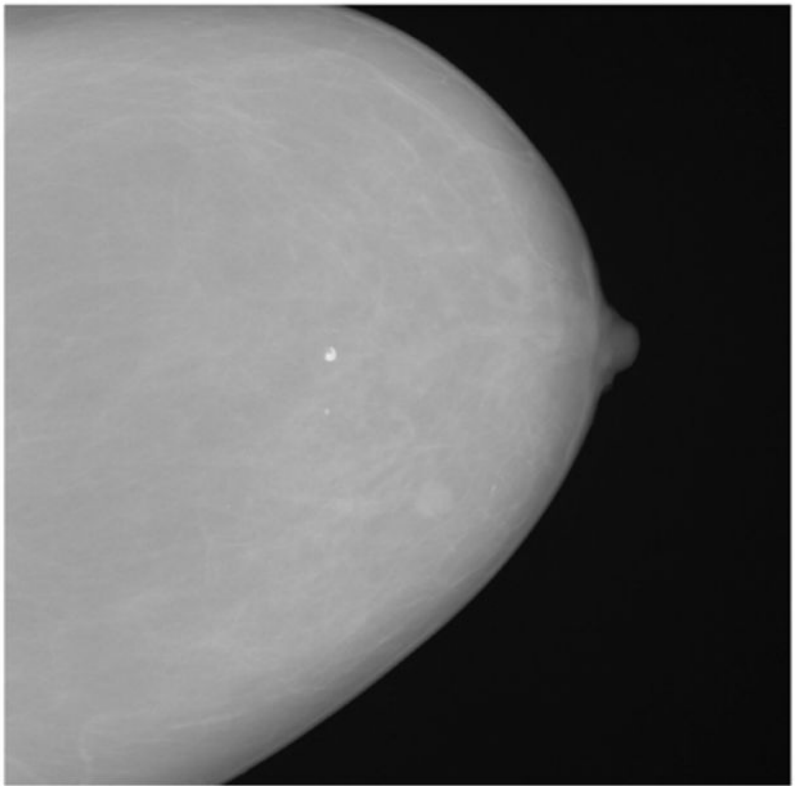

Figure 13.
Low dose middle projection image of a human breast

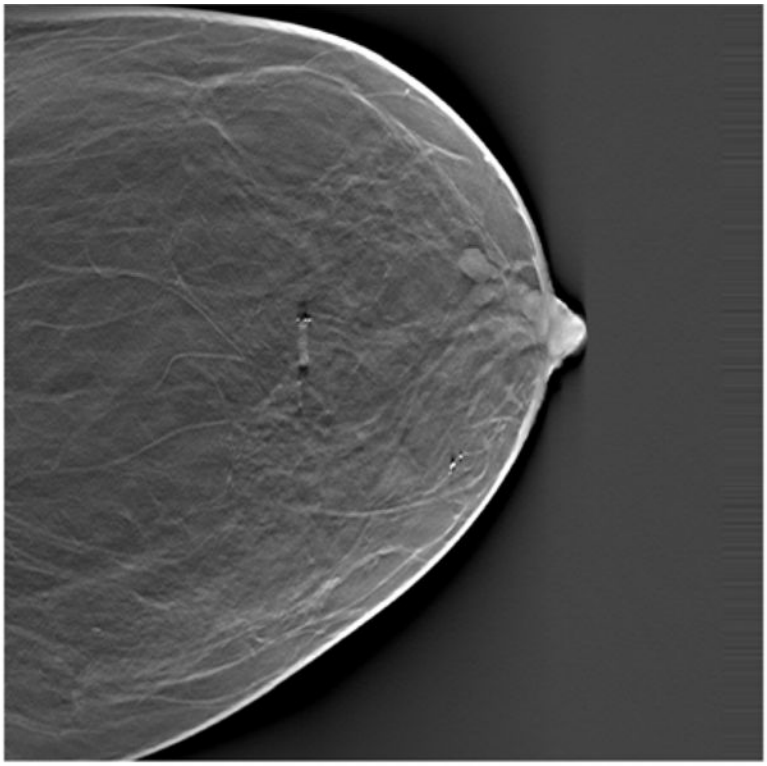

Figure 14.
Filter Back Projection (FBP) slice image of a human breast: $Z = 7.5$ mm